PCCP

ROYAL SOCIETY OF CHEMISTRY

PAPER

View Article Online
View Journal

Check for updates

Cite this: DOI: 10.1039/d3cp00843f

Spin dynamics of [1,2-$^{13}C_2$]pyruvate hyperpolarization by parahydrogen in reversible exchange at micro Tesla fields†

Austin Browning,[a] Keilian Macculloch,[a] Patrick TomHon,[a] Iuliia Mandzhieva,[a] Eduard Y. Chekmenev,[b] Boyd M. Goodson,[c] Sören Lehmkuhl*[a] and Thomas Theis*[a]

Received 22nd February 2023,
Accepted 28th May 2023

DOI: 10.1039/d3cp00843f

rsc.li/pccp

Hyperpolarization of ^{13}C-pyruvate *via* Signal Amplificaton By Reversibble Exchange (SABRE) is an important recent discovery because of both the relative simplicity of hyperpolarization and the central biological relevance of pyruvate as a biomolecular probe for *in vitro* or *in vivo* studies. Here, we analyze the [1,2-$^{13}C_2$]pyruvate-SABRE spin system and its field dependence theoretically and experimentally. We provide first-principles analysis of the governing 4-spin dihydride-$^{13}C_2$ Hamiltonian and numerical spin dynamics simulations of the 7-spin dihydride-$^{13}C_2$–CH_3 system. The analytical and the numerical results are compared to matching systematic experiments. With these methods we unravel the observed spin state mixing of singlet states and triplet states at microTesla fields and we also analyze the dynamics during transfer from micro-Tesla field to high field for detection to understand the resulting spectra from the [1,2-$^{13}C_2$]pyruvate-SABRE system.

Introduction

The toolbox of magnetic resonance (MR) techniques, including nuclear magnetic resonance (NMR) and magnetic resonance imaging (MRI), is used for a wide range of analyses such as the elucidation of chemical and biological systems, investigation of spin interactions, imaging of physiological structures, and diagnosis of disease states. However, MR techniques are inherently limited by low thermal nuclear spin polarization, where a standard MRI magnet (1.5 T) only measures ~5 out of a million proton spins because of low spin polarization = 5.12×10^{-6}.[1] NMR hyperpolarization overcomes this challenge by shifting nuclear spin populations far away from thermal equilibrium, often resulting in polarization >10%.[2,3] This high nuclear spin polarization level can be exploited to generate hyperpolarized contrast agents for real-time metabolic imaging, enabling tracking of individual molecules and their chemical transformations.[4–10] Pyruvate, a central metabolite in multiple metabolic pathways, can be used to image a wide variety of metabolic disorders.[11,12] For example, the Warburg effect enhances anaerobic glycolysis in cancer cells, resulting in increased conversion of pyruvate to lactate in tumors.[13] Hyperpolarized (HP) pyruvate enables imaging of the dysregulated metabolism, promising early detection of tumors through spectroscopic ^{13}C MRSI, and a number of in-patient studies have been demonstrated.[6,12,14] HP pyruvate is under evaluation in 39 clinical trials to date according to clinicaltrials.gov. All-in-all, HP pyruvate is the leading HP metabolic contrast agent and is heading for near-future clinical translation. A metabolic scan with HP pyruvate is fast (1–2 minutes), and it provides similar molecular-level information to that of fluorodeoxyglucose (FDG) PET tracer, but with the added benefit of using non-ionizing radiation.[9] As a result, HP pyruvate metabolic imaging has the potential to become a next-generation molecular imaging modality.

Pyruvate can be hyperpolarized through a variety of methods.[2,15,16] Parahydrogen (p-H_2) Induced Polarization (PHIP) is a particularly simple hyperpolarization approach with modest demands on instrumentation and accordingly low barriers of entry for labs interested in hyperpolarization.[17–20] One powerful approach is PHIP by Side Arm Hydrogenation (PHIP-SAH). Another compelling approach that avoids the need for hydrogenation is Signal Amplification By Reversible Exchange (SABRE).[1,21] SABRE uses p-H_2 in reversible exchange with a polarization transfer catalyst to directly transfer spin order to a substrate of interest. Additionally, SABRE can directly hyperpolarize nuclei with long relaxation times such as ^{13}C and ^{15}N using micro Tesla magnetic fields

---

[a] Department of Chemistry, North Carolina State University, Raleigh, North Carolina, 27695-8204, USA. E-mail: ttheis@ncsu.edu, slehmku@ncsu.edu
[b] Department of Chemistry, Integrative Biosciences (Ibio), Wayne State University, Karmanos Cancer Institute (KCI), Detroit, Michigan 48202, USA
[c] School of Chemical & Biomolecular Sciences and Materials Technology Center, Southern Illinois University, Carbondale, Illinois 62901, USA

† Electronic supplementary information (ESI) available: Additional experimental details (file type, PDF). See DOI: https://doi.org/10.1039/d3cp00843f

through SABRE-SHEATH (SABRE in SHield Enables Alignment Transfer to Heteronuclei).[22–26] It is noted that recent innovations have also shown that pulse sequences can be used to induce SABRE at a variety of magnetic fields.[27–32] In those studies, it is typically just magnetization on a singular spin that is hyperpolarized, as opposed to a singlet state or other spin states supported by two spins – as detailed here. Recently, this method was expanded to demonstrate direct hyperpolarization of pyruvate, enabling facile transfer of singlet spin order from *p*-H_2 derived hydrides to ^{13}C spins in the [1,2-$^{13}C_2$]pyruvate isotopomer.[16] During SABRE-SHEATH, various forms of spin order can result on the five NMR-active spins of [1,2-$^{13}C_2$]pyruvate. In the initial discussion of this paper, we focus on magnetization and singlet order on the $^{13}C_2$ spin pair. Magnetization describes spin polarization aligned with the magnetic field and affected by standard T_1 relaxation, whereas the singlet state describes a symmetry-protected spin state protected from relaxation mechanisms that have identical effect on both spins, as long as the ^{13}C-^{13}C *J*-coupling remains the dominant interaction over other coherent interactions such as a chemical shift difference, or out-of-pair *J*-couplings. Therefore, singlet states often represent long-lived spin states (LLSS) used for storage of hyperpolarized spin order.[33,34] Previous work demonstrated the feasibility of hyperpolarizing various spin states, including the singlet state in [1,2-$^{13}C_2$]pyruvate.[16,35] In this paper, we study the spin dynamics leading to the formation of hyperpolarized spin order on [1,2-$^{13}C_2$]pyruvate, with the goal of maximizing efficiency and reproducibility for future applications of HP pyruvate and related spin systems. First, we provide fundamental (analytical) spin physics analysis of the 16 × 16 Hamiltonian governing the dihydride-$^{13}C_2$ four spin system.[36,37] Then we expand the analysis by numerical simulation of the 7-spin system including the CH_3 group using the SPINACH simulation toolkit, also accounting for effects of reversible exchange.[38] Next, we compare the simulated results to experimental data detailing the effects of the various spin states. Detailed sweeps of the [1,2-$^{13}C_2$]pyruvate SABRE-SHEATH polarization transfer field (PTF) reveal the various optimum fields and matching conditions for creation of singlet order, magnetization, and other spin orders. Finally, we also provide a first-principles analysis of the adiabatic *versus* sudden transfer of the spin system from a micro-Tesla field into the high field of a superconducting magnet, which has major ramifications for the appearance of the NMR spectra.

Experimental

Sample preparation

Under inert gas conditions, [1,2-$^{13}C_2$]pyruvate, Ir(IMes) (IMes = 1,3 bis(2,4,6-trimethylphenyl)imidazole-2-ylidene) catalyst, and DMSO were mixed in a 5 : 1 : 8 ratio, giving absolute concentrations of 15 mM [1,2-$^{13}C_2$]pyruvate, 24 mM DMSO, and 3 mM Ir-IMes) in CD_3OD.[35] All samples were transferred into 7″ medium wall pressure NMR tubes (Wilmad 524-PV-7). Samples were prepared with stock solutions of the Ir-IMes catalyst (12 mM) and degassed CD_3OD. Ir-IMes catalyst was synthesized using a literature method.[39,40] CD_3OD was used dry from the supplier (Cambridge Isotopes) and degassed using 5 freeze–pump–thaw cycles. All other chemicals were purchased from Millipore Sigma.

All experiments were performed using a previously published pneumatic shuttling system.[41] All experiments were run with 93% *p*-H_2 gas produced with a commercially available *p*-H_2 generator.[42] The sample was activated by bubbling *p*-H_2 through the system for 5 minutes (at 100 psi, 76 sccm, 25 °C) where a color change from yellow to colorless is observed during activation of the precatalyst complex, identifying that the activation is complete. Once activated, the sample underwent repetitive field cycling between low polarization fields and the main magnetic field used for detection (Bruker Ascend 9.4 T with Neo Avance III console), allowing for a delay time of 90 seconds in between each experiment to reestablish thermal equilibrium. To minimize hazards and risk associated with the use of hydrogen gas one has to ensure that the total volume of hydrogen gas used remains under the flammability limit. Open flames in the same room where the experiments are conducted must be avoided.

Field sweep

In this study a broad field sweep was performed from −50 to +50 μT, followed by an in-depth study from −3.6 to 3.6 μT in step sizes of 0.1 μT. The polarization transfer field was established by first degaussing the magnetic shielding (Magnetic Shield Corp) using a DG-10 degaussing unit (Twinleaf LLC), followed by fine adjusting the current in a hand-wrapped single-layer solenoid placed in the shields, as previously described.[41]

Simulations

Simulations were carried out in MATLAB using the SPINACH extension developed by the Kuprov group.[38] The simulation uses *J*-coupling values found in the experiments and those that could not be found experimentally were generated by *ab initio* DFT calculations using FHI-Aims code. Specifically, the *ab initio* DFT calculations calculated the J_{HCnear} and J'_{HCnear} depicted in Fig. 1. The other two *J*-couplings, J_{HCfar} and J'_{HCfar} were generated by matching experimental and simulated spectra. The code for simulation of field-cycled SABRE experiments was developed based on previous work and is provided as supplement.[43] Specifically, we added the capabilities for shuttling and field sweeps. The parameters of the simulation were optimized to mirror the parameters and the design of the experimental field sweeps.

Lifetime studies

The experimental lifetimes, T_S and T_1 of [1,2-$^{13}C_2$]pyruvate were measured at varied storage fields. These experiments were performed by first transferring the sample into the μT polarization transfer field to allow spin-state evolution and hyperpolarization of the 13C spin states. Then the sample was transferred to a storage field for a variable amount of time to allow for relaxation. This process was repeated with variable delay times until the signal was below the noise. (Results are provided in Table 2 accompanied by discussion at the end of the manuscript.)

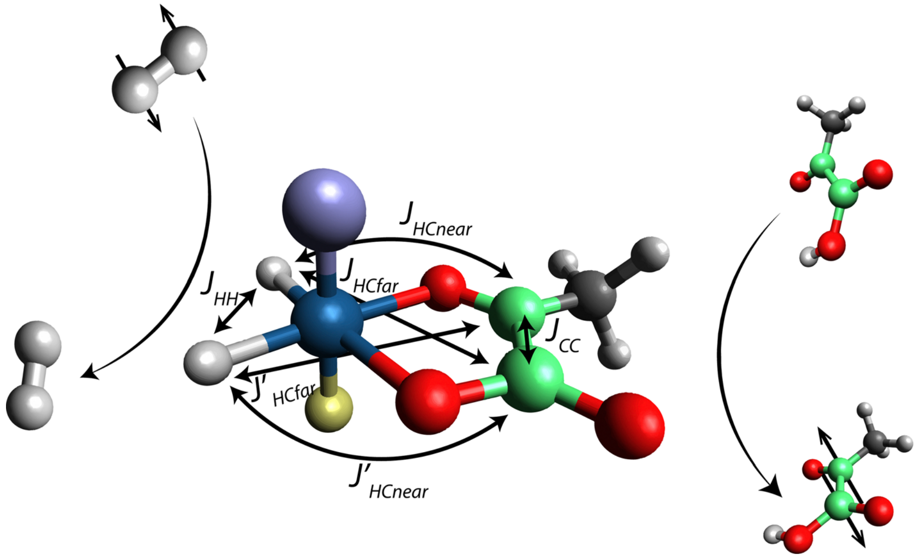

Spin States	PTF (μT)
$\left\|S_0^H T_0^C\right\rangle \rightarrow \left\|T_+^H T_-^C\right\rangle$	0.327
$\left\|S_0^H T_+^C\right\rangle \rightarrow \left\|T_+^H T_0^C\right\rangle$	0.332
$\left\|S_0^H S_0^C\right\rangle \rightarrow \left\|T_-^H T_+^C\right\rangle$	1.550
$\left\|S_0^H T_+^C\right\rangle \rightarrow \left\|T_+^H S_0^C\right\rangle$	2.209

J Couplings	Hz
J_{HH}	-10.6
J_{CC}	59.8
J_{HCfar}	-0.97
J_{HCnear}	-0.50
J'_{HCfar}	-0.06
J'_{HCnear}	0.80

Fig. 1 The active SABRE complex showing the hyperpolarization spin system with the accompanying couplings and relevant spin state transitions. The green orbs show the carbons with their measured 59.8 Hz *J*-coupling; note that this value refers to the bound species, whereas the free species has a *J*-coupling of 62.7 Hz. The light grey orbs show the hydrogens, with the J_{HH} value between hydride spins measured at 10.6 Hz. The inner couplings, J_{HCnear}, J_{HCfar}, J'_{HCnear}, and J'_{HCfar}, could not be extracted from measurements. Instead, they were obtained from *ab initio* calculations and modified to generate agreement with the experimental field dependance of the hyperpolarization field dependance. Accordingly, the error margin on the inner couplings is high. Here only the relevant equatorial ligands are shown with abbreviated axial ligands, with the blue being the iridium center and the purple representing the "IMes" N-heterocyclic carbene ligand (IMes = 1,3 bis(2,4,6-trimethylphenyl)imidazole-2-ylidene). Yellow shows the coligand, DMSO, that is used with the [1,2-$^{13}C_2$]pyruvate system.

Results and discussion

Derivation of spin transfer mechanisms

To understand the details of the [1,2-$^{13}C_2$]pyruvate spin system we examine the possible spin state transitions, where general ideology is adapted from previous studies.[25,36] We begin with the Hamiltonian for the [1,2-$^{13}C_2$]pyruvate Ir dihydride four-spin spin system, as shown in Fig. 1. In this initial discussion, the CH_3 group is omitted as these spins do not significantly impact the polarization process but primarily add additional relaxation pathways, as described towards the end of this manuscript.

The Hamiltonian, H_{tot}, of this four-spin system is represented below with the corresponding operators for the two spins, S for the carbon spins and I for the proton spins:

$$\begin{aligned} H_{\mathrm{tot}} &= \nu_{\mathrm{H}}\left(I_z + I_z^{'}\right) + \nu_{\mathrm{C}}\left(S_z + S_z^{'}\right) \\ &\quad + J_{\mathrm{HH}}\mathbf{I}\cdot\mathbf{I}' + J_{\mathrm{CC}}\mathbf{S}\cdot\mathbf{S}' \\ &\quad + J_{\mathrm{CHnear}}\mathbf{I}\cdot\mathbf{S} + J_{\mathrm{CHnear}}\mathbf{I}'\cdot\mathbf{S} \\ &\quad + J_{\mathrm{CHfar}}\mathbf{I}\cdot\mathbf{S}' + J_{\mathrm{CHfar}}\mathbf{I}'\cdot\mathbf{S}' \end{aligned} \tag{1}$$

where ν_{H} and ν_{c} are the Larmor frequencies for proton and carbon, respectively ($\nu_{\mathrm{H}} = \gamma_{\mathrm{H}}B_0$; $\nu_{\mathrm{c}} = \gamma_{\mathrm{c}}B_0$), and the *J*-couplings correspond to those shown in Fig. 1. I and I' refer to the hydrides, S and S' refer to the carbons. Bolded scalar products, such as $\mathbf{I}{\cdot}\mathbf{S}$ for example are evaluated as $\mathbf{I}{\cdot}\mathbf{S} = I_xS_x + I_yS_y + I_zS_z$. Introducing the sums and the differences of the J_{CH} couplings enables simplified illustration of the Hamiltonian:

$$\begin{aligned} \Delta J_{\mathrm{near}} &= J_{\mathrm{HCnear}} - J_{\mathrm{HCnear}}^{'} \\ \Delta J_{\mathrm{far}} &= J_{\mathrm{HCfar}} - J_{\mathrm{HCfar}}^{'} \\ \sum J_{\mathrm{near}} &= J_{\mathrm{HCnear}} + J_{\mathrm{HCnear}}^{'} \\ \sum J_{\mathrm{far}} &= J_{\mathrm{HCfar}} + J_{\mathrm{HCfar}}^{'} \end{aligned} \tag{2}$$

Eqn (1) and (2) can be combined to give the Hamiltonian as:

$$\begin{aligned} H &= \nu_{\mathrm{H}}(I + I') + \nu_{\mathrm{C}}(S + S') + J_{\mathrm{HH}}\mathbf{I}\cdot\mathbf{I}' + J_{\mathrm{CC}}SS' \\ &\quad + \frac{\sum J_{\mathrm{near}}}{2}(IS + I'S) - \frac{\Delta J_{\mathrm{near}}}{2}(IS - I'S) \\ &\quad + \frac{J_{\mathrm{far}}\sum J_{\mathrm{far}}}{2}(IS' + I'S') - \frac{\Delta J_{\mathrm{far}}}{2}(IS' - I'S') \end{aligned} \tag{3}$$

To analytically dissect this Hamiltonian, we use the traditional singlet–triplet basis for both spin pairs (p-H_2 derived hydrides and ^{13}C pyruvate spins):

$$\begin{aligned} \mathrm{S}_0 &= \frac{1}{\sqrt{2}}|\uparrow\downarrow\rangle - |\downarrow\uparrow\rangle; \\ \mathrm{T}_+ &= |\uparrow\uparrow\rangle; T_0 = \frac{1}{\sqrt{2}}|\uparrow\downarrow\rangle + |\downarrow\uparrow\rangle; T_- = |\downarrow\downarrow\rangle \end{aligned} \tag{4}$$

By finding all possible combinations of the four carbon states with the four hydride states we obtain a total of 16 states that can be divided into symmetric and antisymmetric states.

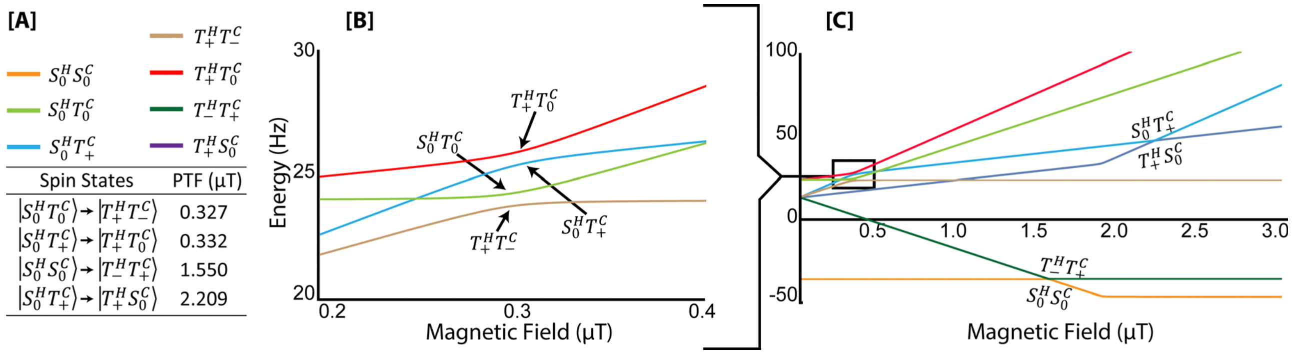

Fig. 2 The level anti-crossings (LACs) for the four-spin [1,2-$^{13}C_2$]pyruvate SABRE complex shown in Fig. 1. The LACs are calculated from equations for a four-spin system. These plots show the relevant spin states starting with a singlet state on the p-H_2 derived hydrides; all other states are omitted for clarity (the full LAC diagram is shown in the ESI†). The calculated fields for the relevant LACs are given in (A). (B) shows a close-up plot (0.2–0.4 μT) of the energy-level curves plotted from 0 to 3 μT (C).

Ten symmetric states are obtained:

$$\begin{aligned} &|S_0^H S_0^C\rangle, |T_0^H T_0^C\rangle,\\ &|T_+^H T_-^C\rangle, |T_-^H T_+^C\rangle,\\ &|T_+^H T_+^C\rangle, |T_-^H T_-^C\rangle, \qquad (5)\\ &|T_0^H T_+^C\rangle, |T_+^H T_0^C\rangle,\\ &|T_0^H T_-^C\rangle, |T_-^H T_0^C\rangle. \end{aligned}$$

And six antisymmetric states are obtained:

$$\begin{aligned} &|S_0^H T_0^C\rangle, |T_0^H S_0^C\rangle,\\ &|S_0^H T_+^C\rangle, |T_+^H S_0^C\rangle, \qquad (6)\\ &|S_0^H T_-^C\rangle, |T_-^H S_0^C\rangle \end{aligned}$$

This basis set enables construction of a full matrix representation of H allowing closer analysis of the transitions between states. The full matrix is provided in the ESI.†[36] To simplify the discussion we focus on individual blocks of the full matrix that describe specific transitions creating hyperpolarization. As p-H_2 is the source of spin order in our system the relevant initial states are those with a S_0^H contribution, initilized through p-H_2 exchange. We expect the four states containing S_0^H to be equally populated initially. We assume zero initial population on all other states when using 100% parahydrogen. Expressed as an equation, The initial density matrix is defined as

$$\rho_i = \frac{1}{4}\hat{1} - (\mathbf{I} \cdot \mathbf{I}'), \qquad (7)$$

where $\mathbf{I}$ and $\mathbf{I}'$ are the angular momentum operators for the two hydrides on the Iridium complex.

We analyze the hyperpolarization dynamics in two ways: first, we simply find the eigenvalues of the total Hamiltonian as a function of magnetic field, which gives us the opportunity to identify the Level Anti Crossings (LACs) at which transitions are likely to occur. Subsequently, we use Bloch Sphere representations to describe the dynamics at (or close to) the identified LACs.

Fig. 2 depicts the energies of the relevant spin states as a function of magnetic field up to 3 μT. We focus on the states with S_0^H contribution and analyze their interactions with other states. In the case of interactions between spin states, avoided crossings are observed as highlighted.

We note that for simplicity, we also omitted the $|S_0^H T_-^C\rangle$ curve in Fig. 2 because it acts just like $|S_0^H T_+^C\rangle$ with inverted symmetry. The full graph with all states is provided in the ESI.†

The points at which avoided crossings are observed identify the positions of interacting spin states. Transitions between those states lead to hyperpolarization transfer. In Fig. 2, the avoided crossings are highlighted by arrows. Generally, the analysis of LACs are ideal for the examination of slow, adiabatic processes and for the present system this LAC analysis provides a good idea of where such transitions are most likely to be efficient.[44] As illustrated in Fig. 2, the identified fields at which the relevant states mix are, 0.327, 0.332, 1.550 and 2.209 μT.

After identifying the magnetic fields through the analysis of LACs (diagonalization of the full Hamiltonian at every field), we return to individual blocks in the Hamiltonian that govern the dynamics between the respective states (obtained in the singlet–triplet basis, *i.e.* diagonalization limited to the J_{HH} and J_{CC} interactions). This may be preferrable because the singlet state on the hydrides is initiated non-adiabatically (*i.e.* suddenly) as expected from a chemical step that is much faster than any spin dynamics. Specifically, the insertion of a fresh parahydrogen molecule into the complex will be fast compared to any J-coupling evolution. Such sudden processes are better represented in Bloch-spheres, where the Hamiltonian and the density matrix are not aligned at all times (as is the case in an adiabatic process). If the density matrix and the Hamiltonian are at an angle with respect to each other, then the resulting evolution is a rotation of the density matrix around the Hamiltonian. We note that if the Hamiltonian and the density matrix were already aligned in the beginning, and without magnetic field cycling, there would be no spin evolution, and no polarization transfer. In the constant field case, the off-diagonal elements are required for polarization transfer. We use this general insight to visualize the pyruvate hyperpolarization dynamics in Bloch Spheres.

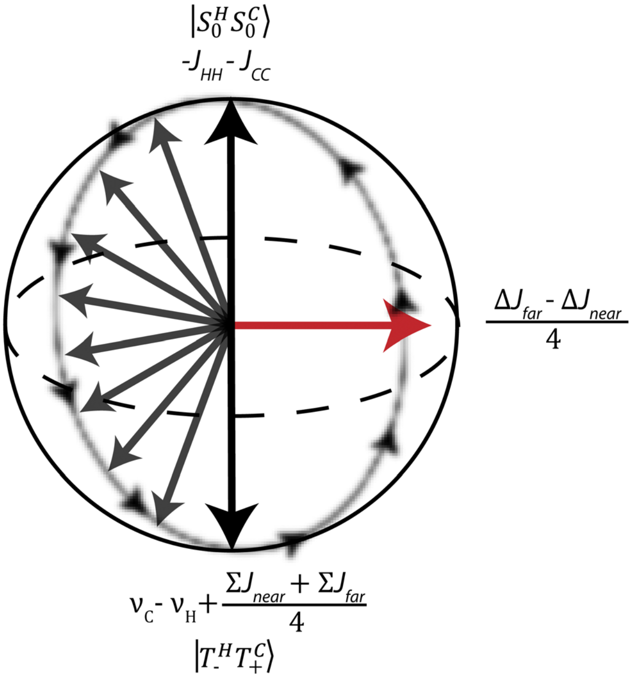

Fig. 3 Bloch Sphere representation of the spin state transfer, depicting the transition of $|S_0^H S_0^C\rangle$ to $|T_-^H T_+^C\rangle$ With on-diagonal terms shown at the top and the bottom with their corresponding states, and the off-diagonal term that connects the two states shown to the right with the red arrow.

Generation of magnetization

First, we examine the generation of magnetization on the [1,2-$^{13}C_2$]pyruvate spins, examining the spin state transition from $|S_0^H S_0^C\rangle$ to $|T_-^H T_+^C\rangle$. The relevant block in the Hamiltonian is:

$$\begin{array}{c c} & \begin{array}{cc} \quad |S_0^H S_0^C\rangle \quad & \quad |T_-^H T_+^C\rangle \end{array} \\ \begin{array}{c} |S_0^H S_0^C\rangle \\[2em] |T_-^H T_+^C\rangle \end{array} & \begin{pmatrix} -J_{HH} - J_{CC} & \dfrac{\Delta J_{far} - \Delta J_{near}}{4} \\ \dfrac{\Delta J_{far} - \Delta J_{near}}{4} & \nu_C - \nu_H + \dfrac{\sum J_{near} + \sum J_{far}}{4} \end{pmatrix} \end{array} \tag{8}$$

The on-diagonal elements primarily determine the distance between the energy levels. When that distance is minimized, a 90° angle is established between the initial density matrix and the Hamiltonian, making population transfer most efficient. We can experimentally control the magnetic field, which determines $\nu_H = \gamma_H B_0$ and $\nu_C = \gamma_C B_0$. Therefore, control of the magnetic field adjusts the position of the energy levels. Note, the J-couplings are not dependent on magnetic field. So, by adjusting the magnetic field, we can optimize the matching condition for population transfer between states. The off-diagonal elements represent the interactions that drive polarization transfer. Their size determines the rate at which the transfer occurs when the diagonal elements are equal to each other.

As illustrated in Fig. 3, the Bloch Sphere shows a visualization of the spin state transitions and their resonance terms. The black arrows represent the precession of the density matrix from one state to another, where the initial state is pure $|S_0^H S_0^C\rangle$ and the final state is $|T_-^H T_+^C\rangle$. The red arrow represents the Hamiltonian in the case of equal diagonal elements. Accordingly, the Hamiltonian has no z-component and that the off-diagonal elements (x-component) are the only active interactions driving the transitions.

To calculate the magnetic field where the energies of the $|S_0^H S_0^C\rangle$ and $|T_-^H T_+^C\rangle$ are matched, and consequently where polarization transfer is most efficient, we set the on-diagonal elements equal to each other:

$$(\nu_H - \nu_C) = J_{HH} + J_{CC} + \frac{\sum J_{near} + \sum J_{far}}{4} \tag{9}$$

The only terms that are easy to manipulate experimentally in this equation are the frequencies ν_H and ν_C, which can be adjusted by changing the magnetic field. Specifically, the frequency difference of ν_H and ν_C depends on the magnetic field as:

$$(\nu_H - \nu_C) = B_{PTF}\,(\gamma_H - \gamma_C) \tag{10}$$

where γ_H and γ_C are the gyromagnetic ratios of protons and carbon nuclei, respectively. Inserting this relationship and solving for the ideal polarization transfer field, B_{PTF}, we obtain:

$$B_{PTF} = \frac{J_{HH} + J_{CC} + \dfrac{\sum J_{near} + \sum J_{far}}{4}}{(\gamma_H - \gamma_C)} \tag{11}$$

Substituting in the known terms and solving for the polarization transfer field yields a B_{PTF} of 1.550 μT. This result is consistent with the evaluation of the LACs above (where the full Hamiltonian was diagonalized, including small J-couplings and fields).

In general, all spin transitions populating magnetization on ^{13}C, *i.e.* $|T_+^C\rangle$ or $|T_-^C\rangle$ are dependent on frequency terms, therefore these transitions can be accessed by changing the applied field. However, in the context of this work, we are also particularly interested in populating $|S_0^C S_0^C\rangle$, the singlet state of the [1,2-$^{13}C_2$]pyruvate, which is not dependent on magnetic fields. For example, examining the matrix block illustrating the $|S_0^H T_0^C\rangle$ to $|T_0^H S_0^C\rangle$ transition where population is generated on the S_0 state of the ^{13}C spins appears as:

$$\begin{array}{c c} & \begin{array}{cc} \quad |S_0^H T_0^C\rangle \quad & \quad |T_0^H S_0^C\rangle \end{array} \\ \begin{array}{c} |S_0^H T_0^C\rangle \\[2em] |T_0^H S_0^C\rangle \end{array} & \begin{pmatrix} -J_{HH} & \dfrac{\Delta J_{near} - \Delta J_{far}}{4} \\ \dfrac{\Delta J_{near} - \Delta J_{far}}{4} & -J_{CC} \end{pmatrix} \end{array} \tag{12}$$

which does not contain magnetic field dependent terms. Here the resonance condition is

$$J_{HH} = J_{CC}. \tag{13}$$

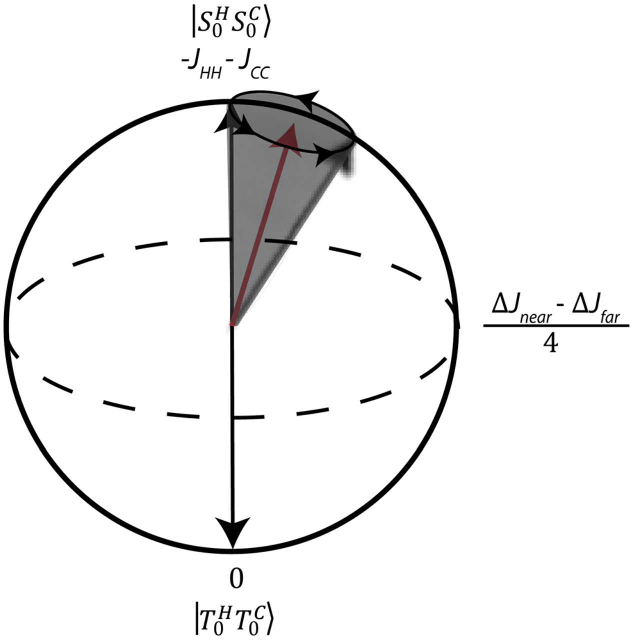

Fig. 4 Bloch sphere representation of the spin state transfer, depicting the transition of $|S_0^H S_0^C\rangle$ to $|T_0^H T_0^C\rangle$ With on-diagonal terms shown on the top and the bottom with their corresponding states and the off-diagonal term that connects the two states shown to the right with the red arrow.

Similarly, the $|S_0^H S_0^C\rangle$ to $|T_0^H T_0^C\rangle$ transition, which acts to deplete $|S_0^C\rangle$, has the following form:

$$\begin{array}{c} \\ |S_0^H S_0^C\rangle \\ |T_0^H T_0^C\rangle \end{array} \begin{array}{c} \begin{array}{cc} |S_0^H S_0^C\rangle & |T_0^H T_0^C\rangle \end{array} \\ \begin{pmatrix} -(J_{HH} + J_{CC}) & \frac{\Delta J_{near} - \Delta J_{far}}{4} \\ \frac{\Delta J_{near} - \Delta J_{far}}{4} & 0 \end{pmatrix} \end{array} \tag{14}$$

also free of magnetic field dependent terms. The resonance condition for this transition is

$$J_{HH} = -J_{CC} \tag{15}$$

For $^{13}C_2$-pyruvate $J_{HH} = -10.6$ Hz and $J_{CC} = +59.8$ Hz, therefore the difference between diagonal elements in eqn (13) is 70.4 Hz, whereas for eqn (15) the difference is 49.2 Hz. Accordingly, the second resonance condition of eqn (15) is slightly more active. However, for the case of $^{13}C_2$ pyruvate neither one of these transitions is going to be particularly strong because the difference in the diagonal elements overwhelms the off-diagonal elements, which are on the order a few Hz. The dynamics of such a case are illustrated in Fig. 4. As can be seen the density matrix never fully inverts in the Bloch-Sphere because the Hamiltonian is not at a 90° angle with respect to the initial density matrix. Accordingly, population transfer remains inefficient.

Because in both of these cases there are no frequency terms that depend on the B_{PTF}, these transitions are only slightly active over a relatively wide magnetic field range from μT to mT magnetic fields.

Table 1 Derived spin state transitions starting from the parahydrogen derived singlet (S_0) state on the hydrides

Spin states	PTF (μT) under LAC conditions	PTF (μT) under Bloch conditions
$|S_0^H T_0^C\rangle \rightarrow |T_+^H T_-^C\rangle$	0.32767	0.32688
$|S_0^H T_+^C\rangle \rightarrow |T_+^H T_0^C\rangle$	0.33444	0.33261
$|S_0^H S_0^C\rangle \rightarrow |T_-^H T_+^C\rangle$	1.55013	1.54954
$|S_0^H T_+^C\rangle \rightarrow |T_+^H S_0^C\rangle$	2.21054	2.20904

Note that these transitions are only reasonable to consider in the regime where the singlet–triplet basis is a good eigenbasis of the spin system. In other words, only as long as the J-couplings outweigh the Zeeman frequency differences. In the case of $^{13}C_2$-pyruvate, the frequency difference of the two ^{13}C nuclei is given by $\Delta\nu = \gamma_{13C} B_0 \cdot \Delta\delta$, where the chemical shift difference $\Delta\delta = 33$ ppm. Above a B_0 of 0.17 T the frequency difference of the two carbons exceeds the J-couplings and the $^{13}C_2$ singlet state is no longer close to an eigenstate of the system and will immediately decohere at fields above this magnetic field threshold.

Although the transitions of eqn (12) and (14) do produce small amounts of singlet polarization, other strongly magnetic-field-dependent transitions can be used to generate singlet hyperpolarization more efficiently. Specifically, one additional matrix block that generates singlet state polarization on the ^{13}C spins with field-dependent terms is given as:

$$\begin{array}{c} \\ |S_0^H T_+^C\rangle \\ |T_+^H S_0^C\rangle \end{array} \begin{array}{c} \begin{array}{cc} |S_0^H T_+^C\rangle & |T_+^H S_0^C\rangle \end{array} \\ \begin{pmatrix} -(J_{HH} + \nu_{CC}) & \frac{\Delta J_{near} - \Delta J_{far}}{4} \\ \frac{\Delta J_{near} - \Delta J_{far}}{4} & -J_{CC} + \nu_H \end{pmatrix} \end{array} \tag{16}$$

Proceeding as in the previous cases, we find the matching condition by setting the diagonal elements equal to each other:

$$\begin{aligned} -J_{HH} + \nu_C &= -J_{CC} + \nu_H \\ B_{PTF} &= \frac{-J_{HH} + J_{CC}}{(\gamma_H - \gamma_C)} \end{aligned} \tag{17}$$

Here, solving for the B_{PTF} value shows that maximum spin transfer into the $T_+^H S_0^C$ state occurs at around 2.209 μT. Using the mathematical analysis described above, we collect the identified fields in Table 1 showing the B_{PTF} optima for each transition, starting in the S_0 state on the p-H_2 derived hydrides using the full derivation. Table 1 also shows the LAC approximations by calculating the crossing points shown in Fig. 2. The PTF values calculated under "LAC" conditions and under "Bloch" conditions differ slightly because under the "LAC" approach the full Hamiltonian is diagonalized, whereas under the "Bloch-sphere" approach (small) off-diagonal elements remain intact, which alter the identified PTFs slightly.

The analytical derivation of these B_{PTF} values does not take exchange mechanisms, (or magnetic field inhomogeneities) into account. Due to exchange, there will be a broader, more distributed efficiency of polarization in the target spin state around the optimal B_{PTF} values.[44,45] Furthermore, the broadening leads to overlapping of transitions, producing non-pure spin states as reflected in experimental spectra that will be discussed below accompanied by numerical simulations.

Analytical consideration of field cycling to high field for detection

To enable comparison between theoretical predictions and experiment it is also critical to account for the processes during sample transfer from μT field to high field for detection. In particular, the frequency difference between the two ^{13}C nuclei, given by $\Delta\nu = \gamma_{13\text{C}}B_0\cdot\Delta\delta$ increases with increasing magnetic field changing the density matrix.

For the analytical analysis of the field cycle, we restrict ourselves to the $^{13}\text{C}_2$ spin pair of the free [1,2-$^{13}\text{C}_2$] pyruvate which can be in one of the states S_0^{C}, T_+^{C}, T_0^{C} or T_-^{C} or a combination thereof. T_+^{C} and T^{C} are eigenstates of, both, the J-coupling Hamiltonians dominant at low field and the strong magnetic field Hamiltonian dominant at typical detection fields (9.4 T here). So, T_+^{C} and T_-^{C} populations are not expected to change during transfer. However, S_0^{C} and T_0^{C} populations will change during field cycling to high field. Here we detail the analysis for the S_0^{C} state and briefly present the analogous results for the T_0^{C} state.

The singlet state $|\alpha\beta - \beta\alpha\rangle/\sqrt{2}$, is not an eigenstate at high magnetic fields. To analyze the dynamics during the adiabatic transfer from μT fields to 9.4 T detection fields, we assume that the density matrix remains an eigenstate of the Hamiltonian, and therefore we analyze the field dependent Hamiltonian.

$$H = J(\mathbf{I}\cdot\mathbf{S}) + \nu_1 I_z + \nu_2 S_Z \tag{18}$$

and calculate the eigenstates of this Hamiltonian as a function of the frequency difference between the ^{13}C nuclei ($\Delta\nu$). For the singlet state one obtains:

$$|\text{eigenstate}(\Delta\nu)\rangle = \frac{\sqrt{\Delta\nu^2 + J_{\text{CC}}{}^2} - \Delta\nu}{J_{\text{CC}}}|\alpha\beta - \beta\alpha\rangle \tag{19}$$

When the singlet, ρ_s, is tested against the two extremes, $\Delta\nu = 0$ (*i.e.* zero-field) this expression gives $|\alpha\beta - \beta\alpha\rangle$, whereas $\Delta\nu = \infty$ (high field) it gives $-|\beta\alpha\rangle$. Similarly, we can also determine the field dependent density matrix under the assumption of a purely adiabatic transfer, where the population remains in the eigenstates of the Hamiltonian at all times (*i.e.* all fields) by evaluating:

$$\rho(\Delta\nu) = |\text{eigenstate }(\Delta\nu)\rangle\langle\text{eigenstate }(\Delta\nu)| \tag{20}$$

where, with $\Delta\nu$ initially set to 0, we obtain:

$$\rho_{0\text{s}} = \frac{1}{4}\hat{1} - \left(S_{1z}S_{2z} + S_{1x}S_{2x} + S_{1y}S_{2y}\right) \tag{21}$$

By raising the magnetic field adiabatically, the density matrix evolves into:

$$\begin{aligned}\rho_s(\Delta\nu) &= \frac{1}{4}\hat{1} - (S_{1z}S_{2z}) - \frac{J_{\text{CC}}}{\sqrt{\Delta\nu^2 + J_{\text{CC}}{}^2}}(S_{1x}S_{2x} + S_{1y}S_{2y}) \\ &\quad - \frac{\Delta\nu}{\sqrt{\Delta\nu^2 + J_{\text{CC}}{}^2}}\frac{1}{2}(S_{1z} - S_{2z})\end{aligned} \tag{22}$$

To further simplify this equation, we introduce the angle θ as $\tan(\theta) = \Delta\nu/J$ and generate the following expression, detailed in

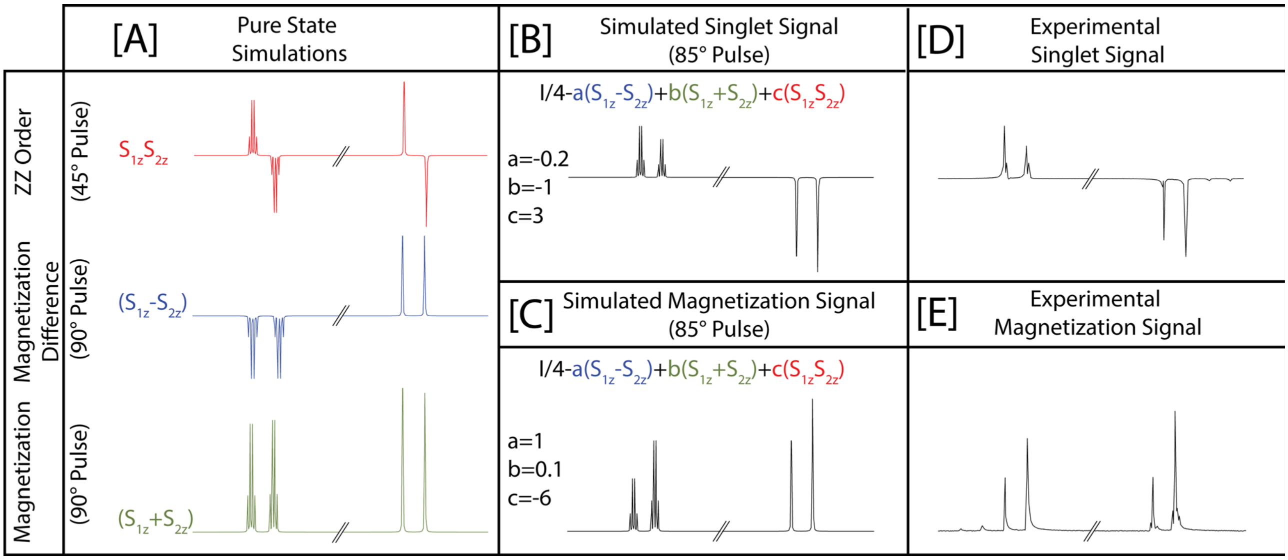

Fig. 5 Simulations of sample transfer spin dynamics and associated spectra. The pure states of $S_{1z}S_{2z}$ (*zz*-order), $S_{1z} + S_{2z}$ (magnetization), and $S_{1z} - S_{2z}$ are shown on the left along with the employed pulse angles for detection. It is noted that for the $S_{1z}S_{2z}$ order a 45-degree pulse is used because *ZZ* order is magnetically silent after a pure 90-degree pulse. The mixed state denoted $I/4 - a(S_{1z} - S_{2z}) + b(S_{1z} + S_{2z}) + c(S_{1z}S_{2z})$ takes into account the pure states with relative coefficients to allow for "matching" between simulated and experimentally observed signals. The experimental results of a singlet and a magnetization spectrum are shown, and compared to simulated spectra using the indicated parameters (*a*,*b*,*c*). The coefficients were adjusted in their relative size, yet are arbitrary in their summed absolute values. The pulse was adjusted to 85 degrees because $S_{1z}S_{2z}$ contribution is observed in the experimental spectra.

the accompanying Mathematica notebook:

$$\begin{aligned}\rho_{\mathrm{s}}(\theta) &= \frac{1}{4}\hat{1} - (S_{1z}S_{2z}) - \cos(\theta)(S_{1x}S_{2x} + S_{1y}S_{2y}) \\ &\quad - \frac{1}{2}\sin(\theta)(S_{1z} - S_{2z})\end{aligned} \tag{23}$$

If we take this analysis to the high-field extreme of $\Delta\nu \to \infty$ (or $\theta = \pi/2$) then we obtain:

$$\rho_{\infty \mathrm{s}} = \frac{1}{4}\hat{1} - (S_{1z}S_{2z}) - \frac{1}{2}(S_{1z} - S_{2z}) \tag{24}$$

This result corresponds to a pure population of $|\beta\alpha\rangle$ that is observable at high fields. When a 90° pulse is applied for readout, only the $S_{1z} - S_{2z}$ component gives signal, resulting in the antiphase peaks shown as the blue trace in Fig. 5A. Meanwhile, the $S_{1z}S_{2z}$ component will contribute to the signal at other flip angles. The $S_{1z}S_{2z}$ contribution to the signal is maximized under a 45° pulse and is shown in the red trace of Fig. 5A.

In contrast, magnetization associated with populations of T_+ ($\rho_{\mathrm{m}+}$) and T_- ($\rho_{\mathrm{m}-}$), which are eigenstates of the Hamiltonian at low and at high field. Therefore, magnetization remains unaffected during field cycling.

$$\rho_{0\mathrm{m}+} = |T_+\rangle\langle T_+| = (S_{1z} + S_{2z}) = |\alpha\alpha\rangle\langle\alpha\alpha| = \rho_{\infty\mathrm{m}+} \tag{25}$$

$$\rho_{0\mathrm{m}-} = |T_-\rangle\langle T_-| = (S_{1z} - S_{2z}) = |\beta\beta\rangle\langle\beta\beta| = \rho_{\infty\mathrm{m}-} \tag{26}$$

The effect of field cycling on the different states is illustrated in Fig. 5, where simulations were performed to show the pure spin states and the mixed spin states correlating to experimental results.

In the experimental $^{13}C_2$-pyruvate SABRE process there never is formation of a pure singlet state or magnetization. Instead, each spectrum is a mixture of various contributions as demonstrated in Fig. 5B–E, where the mixed signals are simulated and denoted by:

$$\frac{1}{4}\mathbf{1} - a(S_{1z} - S_{2z}) + b(S_{1z} + S_{2z}) + c(S_{1z}S_{2z}) \tag{27}$$

where a, b, and c are coefficients used to adjust the contribution of each term. For a pure magnetization case coefficients a and c would be 0. For a pure singlet b would be 0.

Experimentally, we observe contributions from all of these terms and to match the experimentally observed spectra with the simulations the tip angle of the pulses also has to be taken into account. Experimentally we see that there is a difference in the peak heights associated with individual ^{13}C nuclei. As apparent from the traces in Fig. 5A, this can only result from contributions of $S_{1z}S_{2z}$ and non-90° pulses. To match the experiments displayed in Fig. 5D and E, an 85° pulse was used in the simulations displayed in Fig. 5B and C.

1,2 $^{13}C_2$ pyruvate SABRE dynamics through numerical simulations

Spinach simulations were implemented to take into account the effect of chemical exchange as well as to understand the effects of the CH_3 group, both of which could not be tackled by the analytical model used in the previous section.

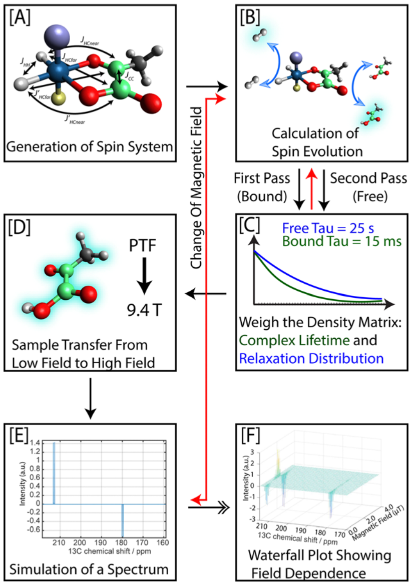

Fig. 6 Computational process for simulating hyperpolarization chemistry and field sweeps of [1,2-$^{13}C_2$]pyruvate. (A) The computation is initiated by defining the spin system by inputting chemical shifts and *J*-couplings. (B) After the spin system is established, we set the B_{PTF} then let the system evolve starting from a singlet state on the hydrides for various evolution times up to 10 s. (C) To take exchange into account, the density matrix of the bound system is exponentially weighted as a function of time (tau =15 ms, characteristic of the exchange, first pass), followed by the decoupling of the hydrides from the spin system, which is followed by another spin evolution period of the free substrate and a second weighting of the density matrix with an exponential (tau =25 s, characteristic of the relaxation). (D) The free substrate is then field cycled up to 9.4 T in small steps to account for the adiabatic nature of the experimental shuttling system. (E) After transition to 9.4 T a $\pi/2$ pulse is applied to generate a spectrum. The code then loops through the same process for the entire B_{PTF} sweep changing the B_{PTF} by increments of 0.1 μT. (F) Finally, the figures are compiled together generating a B_{PTF} swept waterfall plot.

Fig. 6 shows the step-by-step procedure to simulate the entire experimental procedure. The figure caption describes the individual steps and the complete code is provided in the ESI.†

The simulations provide a waterfall plot of simulated spectra, where the hyperpolarization takes place at magnetic fields from 0 to 3.6 μT. The spectral features are consistent with those discussed in the analytical model.

Comparison of experimental and simulated field sweeps

The experimental field sweep is shown in Fig. 7A, and contrasted with the simulated spectra displayed in Fig. 7B. At μT fields the simulation shows only a small amount of perfectly anti-phase signal, whereas in the experiment there is already significant signal observable. This can be attributed to an imperfect demagnetization of the mu-metal shielding, which results in a slight offset of the magnetic field by ∼0.3 μT.

The simulated field sweep, shown in Fig. 7B, does not take any offsets of the magnetic field into account. Generally,

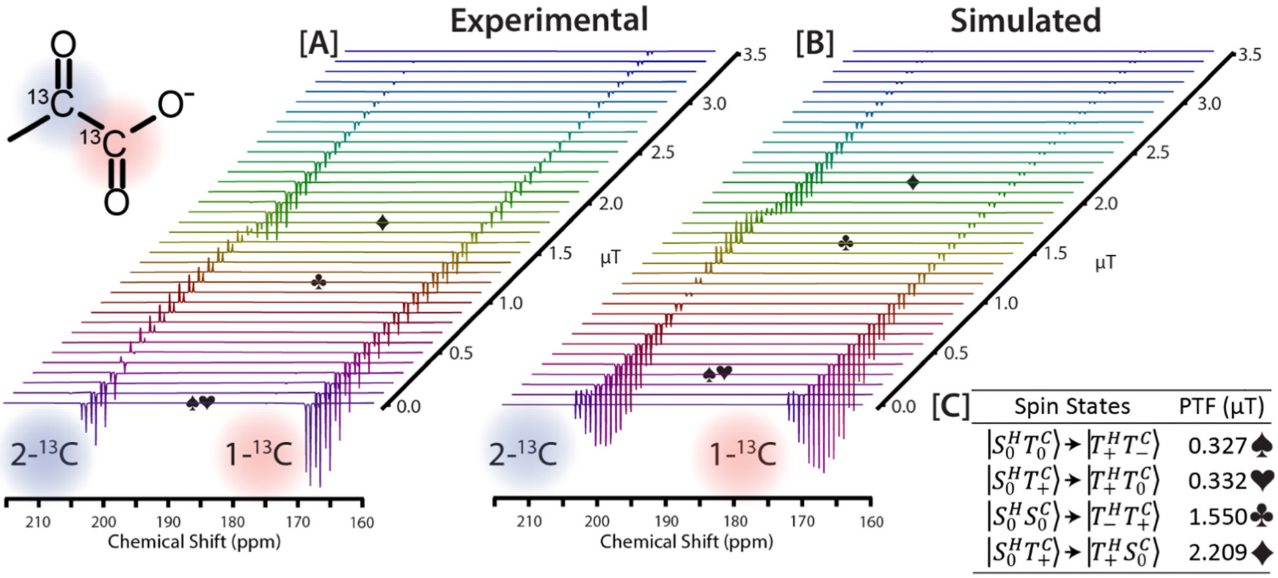

Spin States	PTF (μT)
$\|S_0^H T_0^C\rangle \rightarrow \|T_+^H T_-^C\rangle$	0.327 ♠
$\|S_0^H T_+^C\rangle \rightarrow \|T_+^H T_0^C\rangle$	0.332 ♥
$\|S_0^H S_0^C\rangle \rightarrow \|T_-^H T_+^C\rangle$	1.550 ♣
$\|S_0^H T_+^C\rangle \rightarrow \|T_+^H S_0^C\rangle$	2.209 ♦

Fig. 7 Simulation of the 7-spin dihydride-^{13}C$_2$–CH$_3$ SABRE system *versus* experiment. (A) Experimental and (B) simulated field sweep ^{13}C spectra from 0 to 3.6 μT with 0.1 μT steps. The matching conditions for each are also shown with symbols (spade, heart, club, and diamond) correlating to the positions on the plots (E). Further detailed analysis of this data is provided in Fig. 8.

experiment and simulation are in good agreement with each other, showing the same trends, however slight differences are apparent. Specifically, the experimental magnetic field dependance shows slightly broader features compared to the simulations. Such differences can be attributed to inexact *J*-couplings, especially for the weak couplings. Also, the simulations do not account for faster relaxation on the 2-^{13}C spin, which is closer to the CH$_3$ group and exposed to more relaxation.

In these field sweeps (experimental and simulated), we observe several sign inversions of the hyperpolarized ^{13}C signal, indicative of the changing contributions to the density matrix created as a function of magnetic field. The analytically derived transitions from Table 1 are indicated in Fig. 8, marked by the symbols that identify the corresponding magnetic fields.

The unique shape of the field sweep is due to the mixing of various states at different magnetic fields. As discussed in the previous section, the singlet state can be generated on the [1,2-^{13}C$_2$]pyruvate with low efficiency at any magnetic field, giving rise to a small but constant generation singlet state spin order. To directly connect this numerical simulation to the analytical model, we deconvolute the experimental data to extract the percentage contribution of different spin orders partitioned into singlet spin order *versus* magnetization. Specifically, the intensity difference between 1-^{13}C signal (at 170 ppm) minus 2-^{13}C signal (at 203 ppm) corresponds to singlet order, whereas the sum of 1-^{13}C signal plus 2-^{13}C corresponds to magnetization as illustrated by both experimental and simulated data in Fig. 8.

The difference and the sum of the peaks are calculated and plotted as a function of magnetic field for both, the experiment and the numerical simulation shown in Fig. 8A and B. The offset of ~0.3 μT, in the entire magnetic field sweep, is also apparent in 8A and 8B, as well as the broadening of the magnetic field dependance. Despite minor differences, the general trends let us confirm the identified level anti-crossings. Specifically, the transitions that start with singlet states on the hydrides can now be directly assigned to the magnetic field dependent spectra.

First, marked by ♠, the $|S_0^H T_0^C\rangle \rightarrow |T_+^H T_-^C\rangle$ transitions pumps population into T_-^C, leading to negative magnetization, where both 1-^{13}C and 2-^{13}C peaks point down, while the $|S_0^H T_+^C\rangle \rightarrow |T_+^H T_0^C\rangle$ transition, marked by ♥, gives a loss of T$_c$ population, which also leads to negative magnetization. Since these two transitions are so close together, at 0.327 μT and 0.332 μT respectively, they are active at the same time, both generating negative magnetization. Next, marked by a ♣, the $|S_0^H S_0^C\rangle \rightarrow |T_-^H T_+^C\rangle$ transition pumps population into T_+^C, associated with positive magnetization where both 1-^{13}C and 2-^{13}C peaks point up. In addition, this same transition (♣) leads to a loss of S_0^C, which can be seen as negative singlet signal identified by the amplitude difference of 1-^{13}C and 2-^{13}C signals. Finally, the $|S_0^H T_+^C\rangle \rightarrow |T_+^H S_0^C\rangle$ transition, identified by ♦, entails a gain of S_0^C and a loss of T_+^C. In agreement with this analysis, we observe a maximized singlet signal and a negative magnetization. The individual contributions of the spin states S_0^C, T_0^C, T_+^C, and T_-^C at each magnetic field were also calculated, shown in Fig. 8C. These calculations present the projections of the individual spin state contributions onto the density matrix at every magnetic field during the simulations. From the individual spin states, total magnetization is extracted as T_-^C–T_+^C, agreeing with the spectral analysis used for magnetization in 8B. The total singlet contribution was evaluated as T_0^C–S_0^C, also showing excellent agreement with the spectral analysis for the singlet contribution of 8B. Accordingly, the results from 8C validate the approach taken in 8A and B to extract the relative contributions of singlet and magnetization.

The analysis of these transitions that all start with the singlet on the hydrides, give a clear understanding of the shape of the observed field sweep shown in Fig. 7A and B. By extracting the relative contributions of magnetization and singlet, as depicted

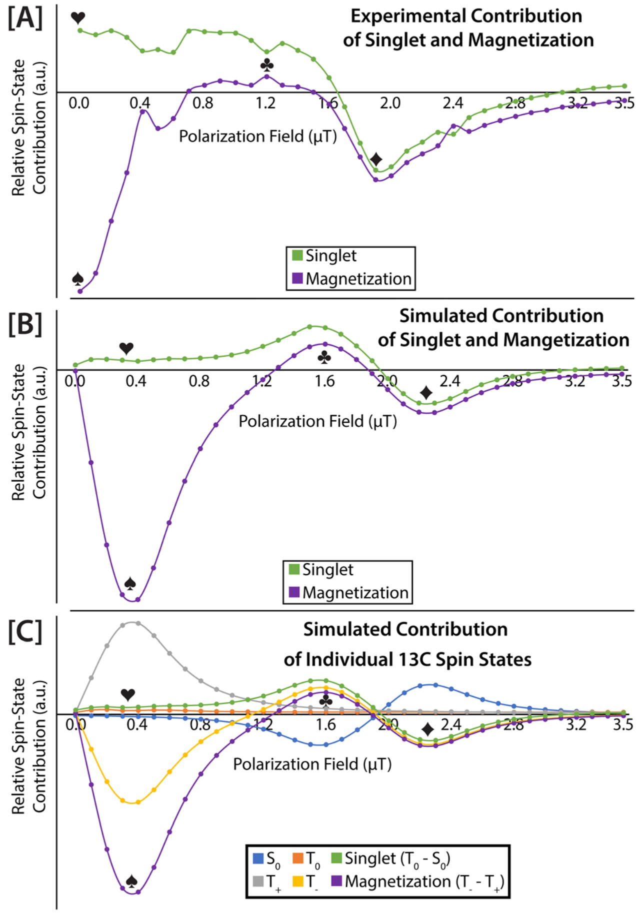

Fig. 8 Percentages of magnetization and singlet character as a function of magnetic field for both (A) experiment and (B) simulation. For A and B, singlet is extracted from experimental and simulated spectra as difference of 1-C amplitude −2-C amplitude, and magnetization as sum of 1-C amplitude +2-C amplitude. (C) The simulated contribution of individual carbon spin states S_0, T_0, T_+, T_-, is extracted from projections of these states onto the density matrix. In C, total singlet is evaluated as $T_0 - S_0$, and magnetization as $T_- - T_+$ to give excellent agreement with the peak amplitude analysis method of A and B.

in Fig. 8A–C, the activity of these transitions can be identified and assigned to the specific magnetic fields and observed spectra.

[1,2-$^{13}C_2$]pyruvate lifetime studies

As fully detailed in the Experimental section, the sample was hyperpolarized at B_{PTF}, in this case 0.8 μT, which was chosen because the singlet polarization is maximized while minimizing magnetization. Then the sample was moved to a storage field so that the sample could undergo hyperpolarization decay for variable time periods. The lifetime of [1,2-$^{13}C_2$]pyruvate in the presence of the SABRE catalyst, both T_1 and T_s were studied and the results are depicted in Fig. 9 and summarized in Table 2. For each resonance the relaxation curve was fit using:

$$S(t) = A \times \mathrm{e}^{\frac{-t+B}{\tau}} \tag{28}$$

where A and B are scaling factors. All individual datasets and their fits are provided in the ESI.† The spectra were analyzed in two ways, first both 1-^{13}C and 2-^{13}C peaks were analyzed separately to determine their individual lifetimes. Secondly, for data below 50 mT, the 1-^{13}C and 2-^{13}C peaks were subtracted from each other to assess T_s.

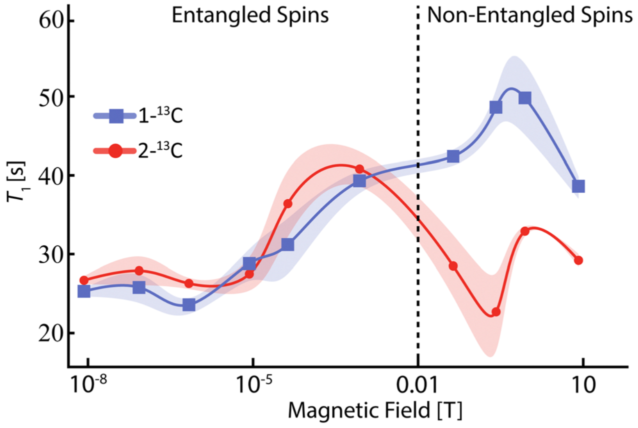

Fig. 9 T_S and T_1 data established by measuring the decay of the 1-^{13}C signal and the 2-^{13}C signal. Up to 50 mT ($J_{\mathrm{CC}} > \delta_{\mathrm{CC}}$) the singlet state relaxation T_S is observed on both peaks because the two spins remain entangled. The same relaxation rate is observed on both spins. Above 170 mT ($J_{\mathrm{CC}} < \delta_{\mathrm{CC}}$), the spins are no longer entangled and experience distinguishable T_1 relaxation rates.

When the frequency difference between 1-^{13}C and 2-^{13}C becomes larger than the J-coupling between them (J_{CC} = 59.8 Hz) the singlet state is no longer an eigenstate of the dominant Hamiltonian. At 170 mT the chemical shift difference is equal to the J_{CC} coupling of 59.8 Hz. As can be seen from Fig. 9 and Table 2, at fields of 50 mT and below, nearly identical relaxation rates are found for the two ^{13}C sites because the entangled singlet state experiences relaxation. At magnetic fields of 300 mT and above the observed relaxation rates begin to deviate as expected for individual spins. In particular, the relaxation of the 2-^{13}C site becomes faster than that of the 1-^{13}C position because the dipolar relaxation induced by the CH_3 group at the 2-^{13}C site can be expected to be much larger than the dipolar effects expected at the 1-^{13}C site.

So, the last data point taken for T_s is at 50 mT since the next field, 300 mT, is above the singlet threshold. This change can be seen in the T_1 data as well due to the spins being quantum entangled in the singlet state and separated as the singlet state is broken. The T_1 data shows a close correlation between the

Table 2 Singlet state lifetimes at various storage fields

Magnetic field	T_1 at 1-^{13}C (s)	T_1 at 2-^{13}C (s)	T_S of 1,2-^{13}C (s)
0 μT	25.0 ± 0.5	26.4 ± 0.5	25.9 ± 0.5
0.1 μT	25.5 ± 1.8	27.6 ± 1.8	26.4 ± 1.8
0.8 μT	23.3 ± 1.0	26.0 ± 0.7	24.5 ± 0.9
10 μT	28.5 ± 2.0	27.2 ± 2.1	27.8 ± 2.1
50 μT	30.9 ± 3.5	36.1 ± 4.2	34.3 ± 5.6
1 mT	39.0 ± 1.4	40.5 ± 2.2	39.6 ± 1.4
50 mT	42.1 ± 1.0	28.2 ± 3.9	35.8 ± 2.4
300 mT	48.3 ± 2.4	22.4 ± 4.9	
1 T	49.5 ± 4.5	32.6 ± 0.6	
9.4 T	38.3 ± 1.4	28.9 ± 0.8	

1-^{13}C and 2-^{13}C lifetimes until 50 mT were the 1-^{13}C peak starts decaying at a faster rate than 2-^{13}C.

The maximum T_s lifetime was observed at 1 mT, 39.6 ± 1.4 s, the fitted data is shown in the ESI.† The maximum T_1 lifetime for 1-^{13}C was observed at 1 T, 49.5 ± 4.5, while the maximum T_1 lifetime for 2-^{13}C was observed at 1 mT, 40.5 ± 2.2 s. These measurements were made within the SABRE system, so there are multiple transitions and relaxation effects that can occur at different fields – potentially explaining the trend in the data. The lifetimes observed show an increase in comparison to measured T_1 values in literature.[16] In the present measurements the observed singlet state lifetimes are close to the T_1 times observed on the carbons. We attribute this behavior to the fact that relaxation may be dominated by the dipolar interactions with the CH_3 group. These dipolar interactions are asymmetric with respect to the two carbons and the singlet state is not protected from relaxation caused by asymmetric interactions that act differently on the two carbons.

Conclusion

In this study we performed a complete theoretical analysis of [$^{13}C_2$]pyruvate singlet hyperpolarization *via* SABRE and compared the theoretical results to experiments. The theoretical analysis starts with the analytical expressions for the relevant, field-dependent Hamiltonians. First the Level-Anti Crossing (LAC) positions were identified by diagonalizing the entirety of the Hamiltonian. Second, at those LAC positions the polarization transfer dynamics were studied by analyzing blocks of the Hamiltonian in a singlet–triplet basis. This analysis allows for a depiction of the polarization transfer dynamics as simple rotations on Bloch-spheres giving a more intuitive access to understanding SABRE. Next, in order to model the field cycling process, in which the sample goes from a μT field to a high magnetic field for detection, first-principles mathematics were developed that give an analytical solution of the resulting density matrix at high field in case of an adiabatic transfer from low to high field. After establishing the first-principles analytical concepts, we implemented numerical simulations that are able to take exchange and relaxation into account, but more importantly the numerical simulations could handle larger spin systems such that effects of the CH_3 group in pyruvate could also be studied, allowing for more detailed comparisons with experiment.

The Analysis of the four-spin [1,2-$^{13}C_2$]pyruvate SABRE system illustrates four main transitions that occur with an initial singlet state on the p-H_2 derived hydrides, resulting in the accumulation of either magnetization or singlet state spin order on the [1,2-$^{13}C_2$]pyruvate ^{13}C spin pair originating from the different transitions active at different magnetic fields.

Each analytically identified transition was found to have corresponding features in, both, the numerically simulated and the experimental field sweeps. Finally, the observed ^{13}C peak patterns were analyzed in detail confirming that there is a field-independent mechanism creating S_0 signal along with field-dependent mechanisms for population of the T_+, T_-, T_0, and S_0 states of the ^{13}C spins.

The detailed understanding conveyed in this paper could be used, when paired with experiments and simulations, to describe and develop the hyperpolarization of novel target molecules and new SABRE catalysts.

Disclaimer

This report was prepared as an account of work sponsored by an agency of the United States Government. Neither the United States Government nor any agency thereof, nor any of their employees, makes any warranty, express or implied, or assumes any legal liability or responsibility for the accuracy, completeness, or usefulness of any information, apparatus, product, or process disclosed, or represents that its use would not infringe privately owned rights. Reference herein to any specific commercial product, process, or service by trade name, trademark, manufacturer, or otherwise does not necessarily constitute or imply its endorsement, recommendation, or favoring by the United States Government or any agency thereof. The views and opinions of authors expressed herein do not necessarily state or reflect those of the United States Government or any agency.

Conflicts of interest

Thomas Theis, Eduard Chekmenev and Patrick TomHon hold shares of Vizma Life Sciences (VLS). TT and EC serve on the Scientific Advisory Board of VLS; PT is and employee of VLS. VLS develops products related to the research being reported. The terms of this arrangement have been reviewed and approved by NC State University in accordance with its policy on objectivity in research. BMG and EYC declare stake ownership in XeUS Technologies, Ltd.

Acknowledgements

Research reported in this publication was supported by the National Institute of Biomedical Imaging and Bioengineering of the National Institutes of Health under Award no. NIH R21EB025313 and NIH R01EB029829. The content is solely the responsibility of the authors and does not necessarily represent the official views of the National Institutes of Health. In addition, we acknowledge funding from the Mallinckrodt Foundation, the National Science Foundation under Awards CHE-1905341 and CHE-1904780, and from the North Carolina Biotechnology Center in the form of a Translational Research Grant. Finally, we would like to acknowledge the support from NCSU's METRIC providing access to NMR instrumentation. This material is based upon work supported by the U.S. Department of Energy, Office of Biological and Environmental Research (BER) under Award Number(s) DE-SC0023334.

Notes and references

1 D. A. Barskiy, S. Knecht, A. V. Yurkovskaya and K. L. Ivanov, SABRE: Chemical kinetics and spin dynamics of the formation of hyperpolarization, *Prog. Nucl. Magn. Reson. Spectrosc.*, 2019, **114–115**, 33–70.

2 J. H. Ardenkjær-Larsen, B. Fridlund, A. Gram, G. Hansson, L. Hansson, M. H. Lerche, R. Servin, M. Thaning and K. Golman, Increase in signal-to-noise ratio of >10,000 times in liquid-state NMR, *Proc. Natl. Acad. Sci. U. S. A.*, 2003, **100**, 10158–10163.

3 P. Nikolaou, B. M. Goodson and E. Y. Chekmenev, NMR hyperpolarization techniques for biomedicine, *Chem. – Eur. J.*, 2015, **21**, 3156–3166.

4 A. Gamliel, S. Uppala, G. Sapir, T. Harris, A. Nardi-Schreiber, D. Shaul, J. Sosna, J. M. Gomori and R. Katz-Brull, Hyperpolarized [^{15}N]nitrate as a potential long lived hyperpolarized contrast agent for MRI, *J. Magn. Reson.*, 2019, **299**, 188–195.

5 E. M. Serrao and K. M. Brindle, Potential clinical roles for metabolic imaging with hyperpolarized [1-^{13}C]pyruvate, *Front. Oncol.*, 2016, **6**, 1–6.

6 S. J. Nelson, J. Kurhanewicz, D. B. Vigneron, P. E. Z. Larson, A. L. Harzstark, M. Ferrone, M. Van Criekinge, J. W. Chang, R. Bok, I. Park, G. Reed, L. Carvajal, E. J. Small, P. Munster, V. K. Weinberg, J. H. Ardenkjaer-Larsen, A. P. Chen, R. E. Hurd, L. I. Odegardstuen, F. J. Robb, J. Tropp and J. A. Murray, Metabolic imaging of patients with prostate cancer using hyperpolarized [1-^{13}C]pyruvate, *Sci. Transl. Med.*, 2013, **5**(198), DOI: **10.1126/scitranslmed.3006070**.

7 K. Golman, J. H. Ardenkjær-Larsen, J. S. Petersson, S. Månsson and I. Leunbach, Molecular imaging with endogenous substances, *Proc. Natl. Acad. Sci. U. S. A.*, 2003, **100**, 10435–10439.

8 M. E. Merritt, C. Harrison, C. Storey, F. M. Jeffrey, A. D. Sherry and C. R. Malloy, Hyperpolarized ^{13}C allows a direct measure of flux through a single enzyme-catalyzed step by NMR, *Proc. Natl. Acad. Sci. U. S. A.*, 2007, **104**, 19773–19777.

9 S. E. Day, M. I. Kettunen, F. A. Gallagher, D. E. Hu, M. Lerche, J. Wolber, K. Golman, J. H. Ardenkjaer-Larsen and K. M. Brindle, Detecting tumor response to treatment using hyperpolarized ^{13}C magnetic resonance imaging and spectroscopy, *Nat. Med.*, 2007, **13**, 1382–1387.

10 K. Golman, O. Axelsson, H. Jóhannesson, S. Månsson, C. Olofsson and J. S. Petersson, Parahydrogen-induced polarization in imaging: subsecond ^{13}C angiography, *Magn. Reson. Med.*, 2001, **46**, 1–5.

11 R. L. Hesketh and K. M. Brindle, Magnetic resonance imaging of cancer metabolism with hyperpolarized ^{13}C-labeled cell metabolites, *Curr. Opin. Chem. Biol.*, 2018, **45**, 187–194.

12 J. Kurhanewicz, D. B. Vigneron, J. H. Ardenkjaer-Larsen, J. A. Bankson, K. Brindle, C. H. Cunningham, F. A. Gallagher, K. R. Keshari, A. Kjaer, C. Laustsen, D. A. Mankoff, M. E. Merritt, S. J. Nelson, J. M. Pauly, P. Lee, S. Ronen, D. J. Tyler, S. S. Rajan, D. M. Spielman, L. Wald, X. Zhang, C. R. Malloy and R. Rizi, Hyperpolarized 13C MRI: Path to Clinical Translation in Oncology, *Neoplasia*, 2019, **21**, 1–16.

13 M. V. Liberti and J. W. Locasale, The Warburg Effect: How Does it Benefit Cancer Cells?, *Trends Biochem. Sci.*, 2016, **41**, 211–218.

14 M. J. Albers, R. Bok, A. P. Chen, C. H. Cunningham, M. L. Zierhut, V. Y. Zhang, S. J. Kohler, J. Tropp, R. E. Hurd, Y. F. Yen, S. J. Nelson, D. B. Vigneron and J. Kurhanewicz, Hyperpolarized ^{13}C lactate, pyruvate, and alanine: noninvasive biomarkers for prostate cancer detection and grading, *Cancer Res.*, 2008, **68**, 8607–8615.

15 F. Reineri, T. Boi and S. Aime, ParaHydrogen Induced Polarization of ^{13}C carboxylate resonance in acetate and pyruvate, *Nat. Commun.*, 2015, **6**, 1–6.

16 W. Iali, S. S. Roy, B. J. Tickner, F. Ahwal, A. J. Kennerley and S. B. Duckett, Hyperpolarising Pyruvate through Signal Amplification by Reversible Exchange (SABRE), *Angew. Chemie*, 2019, **131**, 10377–10381.

17 J. B. Hövener, A. N. Pravdivtsev, B. Kidd, C. R. Bowers, S. Glöggler, K. V. Kovtunov, M. Plaumann, R. Katz-Brull, K. Buckenmaier, A. Jerschow, F. Reineri, T. Theis, R. V. Shchepin, S. Wagner, P. Bhattacharya, N. M. Zacharias and E. Y. Chekmenev, Parahydrogen-Based Hyperpolarization for Biomedicine, *Angew. Chem. Int. Ed.*, 2018, **57**, 11140–11162.

18 A. B. Schmidt, J. B. Hövener, C. R. Bowers, K. Buckenmaier, E. Y. Chekmenev, H. de Maissin, J. Eills, F. Ellermann, S. Glöggler, J. W. Gordon, S. Knecht, I. V. Koptyug, J. Kuhn, A. N. Pravdivtsev, F. Reineri, T. Theis and K. Them, Instrumentation for hydrogenative parahydrogen-based hyperpolarization techniques, *Anal. Chem.*, 2022, **94**, 479–502.

19 C. R. Bowers and D. P. Weitekamp, Transformation of Symmetrization Order to Nuclear-Spin Magnetization by Chemical Reaction and Nuclear Magnetic Resonance, *Phys. Rev. Lett.*, 1986, **57**, 2645.

20 D. O. Zakharov, K. Chernichenko, K. Sorochkina, S. Yang, V.-V. Telkki, T. Repo, V. V. Zhivonitko, D. O. Zakharov, K. Sorochkina, S. Yang, V. Telkki, V. V. Zhivonitko, K. Chernichenko and T. Repo, Parahydrogen-Induced Polarization in Hydrogenation Reactions Mediated by a Metal-Free Catalyst, *Chem. – Eur. J.*, 2022, **28**, e202103501.

21 R. W. Adams, J. A. Aguilar, K. D. Atkinson, M. J. Cowley, P. I. P. Elliott, S. B. Duckett, G. G. R. Green, I. G. Khazal, J. Lopez-Serrano and D. C. Williamson, Sensitivity by Polarization Transfer, *Science*, 2009, **323**, 1708–1711.

22 D. A. Barskiy, R. V. Shchepin, C. P. N. Tanner, J. F. P. Colell, B. M. Goodson, T. Theis, W. S. Warren and E. Y. Chekmenev, The Absence of Quadrupolar Nuclei Facilitates Efficient 13C Hyperpolarization via Reversible Exchange with Parahydrogen, *Chem. Phys. Chem.*, 2017, **18**, 1493–1498.

23 M. L. Truong, T. Theis, A. M. Coffey, R. V. Shchepin, K. W. Waddell, F. Shi, B. M. Goodson, W. S. Warren and E. Y. Chekmenev, ^{15}N Hyperpolarization by Reversible Exchange Using SABRE-SHEATH, *J. Phys. Chem. C*, 2015, **119**, 8786–8797.

24 R. V. Shchepin, M. L. Truong, T. Theis, A. M. Coffey, F. Shi, K. W. Waddell, W. S. Warren, B. M. Goodson and E. Y. Chekmenev, Hyperpolarization of 'Neat' Liquids by NMR Signal Amplification by Reversible Exchange, *J. Phys. Chem. Lett.*, 2015, **6**, 1961–1967.

25 J. F. P. Colell, A. W. J. Logan, Z. Zhou, R. V. Shchepin, D. A. Barskiy, G. X. Ortiz, Q. Wang, S. J. Malcolmson, E. Y. Chekmenev, W. S. Warren and T. Theis, Generalizing, Extending, and Maximizing Nitrogen-15 Hyperpolarization Induced by Parahydrogen in Reversible Exchange, *J. Phys. Chem. C*, 2017, **121**, 6626–6634.

26 T. Theis, M. L. Truong, A. M. Coffey, R. V. Shchepin, K. W. Waddell, F. Shi, B. M. Goodson, W. S. Warren and E. Y. Chekmenev, Microtesla SABRE enables 10% nitrogen-15 nuclear Spin polarization, *J. Am. Chem. Soc.*, 2015, **137**, 1404–1407.

27 S. Knecht, A. S. Kiryutin, A. V. Yurkovskaya and K. L. Ivanov, Re-polarization of nuclear spins using selective SABRE-INEPT, *J. Magn. Reson.*, 2018, **287**, 10–14.

28 A. B. Schmidt, J. Eills, L. Dagys, M. Gierse, M. Keim, S. Lucas, M. Bock, I. Schwartz, M. Zaitsev, E. Y. Chekmenev and S. Knecht, Over 20% Carbon-13 Polarization of Perdeuterated Pyruvate Using Reversible Exchange with Parahydrogen and Spin-Lock Induced Crossing at 50 μT, *J. Phys. Chem. Lett.*, 2023, **14**, 5305.

29 T. Theis, M. Truong, A. M. Coffey, E. Y. Chekmenev and W. S. Warren, LIGHT-SABRE enables efficient in-magnet catalytic hyperpolarization, *J. Magn. Reson.*, 2014, **248**, 23–26.

30 A. N. Pravdivtsev, K. Buckenmaier, N. Kempf, G. Stevanato, K. Scheffler, J. Engelmann, M. Plaumann, R. Koerber, J.-B. Hövener and T. Theis, LIGHT-SABRE Hyperpolarizes [1-^{13}C]Pyruvate Continuously without Magnetic Field Cycling, *J. Phys. Chem. C*, 2023, **16**, 18.

31 S. S. Roy, G. Stevanato, P. J. Rayner and S. B. Duckett, Direct enhancement of nitrogen-15 targets at high-field by fast ADAPT-SABRE, *J. Magn. Reson.*, 2017, **285**, 55–60.

32 S. L. Eriksson, J. R. Lindale, X. Li and W. S. Warren, Improving SABRE hyperpolarization with highly nonintuitive pulse sequences: Moving beyond avoided crossings to describe dynamics, *Sci. Adv.*, 2022, **8**, 3708.

33 A. Bornet, S. Jannin and G. Bodenhausen, Three-field NMR to preserve hyperpolarized proton magnetization as long-lived states in moderate magnetic fields, *Chem. Phys. Lett.*, 2011, **512**, 151–154.

34 B. Meier, J. N. Dumez, G. Stevanato, J. T. Hill-Cousins, S. S. Roy, P. Haìškansson, S. Mamone, R. C. D. Brown, G. Pileio and M. H. Levitt, Long-lived nuclear spin states in methyl groups and quantum-rotor-induced polarization, *J. Am. Chem. Soc.*, 2013, **135**, 18746–18749.

35 B. J. Tickner, O. Semenova, W. Iali, P. J. Rayner, A. C. Whitwood and S. B. Duckett, Optimisation of pyruvate hyperpolarisation using SABRE by tuning the active magnetisation transfer catalyst, *Catal. Sci. Technol.*, 2020, **10**, 1343–1355.

36 T. Theis, G. X. Ortiz, A. W. J. Logan, K. E. Claytor, Y. Feng, W. P. Huhn, V. Blum, S. J. Malcolmson, E. Y. Chekmenev, Q. Wang and W. S. Warren, Direct and cost-efficient hyperpolarization of long-lived nuclear spin states on universal $^{15}N_2$-diazirine molecular tags, *Sci. Adv.*, 2016, **2**, 1–8.

37 Z. Zhou, J. Yu, J. F. P. Colell, R. Laasner, A. Logan, D. A. Barskiy, R. V. Shchepin, E. Y. Chekmenev, V. Blum, W. S. Warren and T. Theis, Long-Lived $^{13}C_2$ Nuclear Spin States Hyperpolarized by Parahydrogen in Reversible Exchange at Microtesla Fields, *J. Phys. Chem. Lett.*, 2017, **8**, 3008–3014.

38 H. J. Hogben, M. Krzystyniak, G. T. P. Charnock, P. J. Hore and I. Kuprov, Spinach - A software library for simulation of spin dynamics in large spin systems, *J. Magn. Reson.*, 2011, **208**, 179–194.

39 M. J. Cowley, R. W. Adams, K. D. Atkinson, M. C. R. Cockett, S. B. Duckett, G. G. R. Green, J. A. B. Lohman, R. Kerssebaum, D. Kilgour and R. E. Mewis, Iridium N-heterocyclic carbene complexes as efficient catalysts for magnetization transfer from parahydrogen, *J. Am. Chem. Soc.*, 2011, **133**, 6134–6137.

40 L. D. Vazquez-Serrano, B. T. Owens and J. M. Buriak, The search for new hydrogenation catalyst motifs based on N-heterocyclic carbene ligands, *Inorganica Chim. Acta*, 2006, **9**, 2786–2797.

41 P. TomHon, E. Akeroyd, S. Lehmkuhl, E. Y. Chekmenev and T. Theis, Automated pneumatic shuttle for magnetic field cycling and parahydrogen hyperpolarized multidimensional NMR, *J. Magn. Reson.*, 2020, **312**, 106700.

42 J. B. Hövener, S. Bär, J. Leupold, K. Jenne, D. Leibfritz, J. Hennig, S. B. Duckett and D. Von Elverfeldt, A continuous-flow, high-throughput, high-pressure parahydrogen converter for hyperpolarization in a clinical setting, *NMR Biomed.*, 2013, **26**, 124–131.

43 S. Lehmkuhl, M. Suefke, A. Kentner, Y. F. Yen, B. Blümich, M. S. Rosen, S. Appelt and T. Theis, SABRE polarized low field rare-spin spectroscopy, *J. Chem. Phys.*, 2020, **152**, 1–9.

44 K. L. Ivanov, A. N. Pravdivtsev, A. V. Yurkovskaya, H. M. Vieth and R. Kaptein, The role of level anti-crossings in nuclear spin hyperpolarization, *Prog. Nucl. Magn. Reson. Spectrosc.*, 2014, **81**, 1–36.

45 A. N. Pravdivtsev, A. V. Yurkovskaya, H. M. Vieth, K. L. Ivanov and R. Kaptein, Level anti-crossings are a key factor for understanding para-hydrogen-induced hyperpolarization in SABRE experiments, *Chem. Phys. Chem.*, 2013, **14**, 3327–3331.